SPE 36491

Laboratory Imaging of Stimulation Fluid Displacment from Hydraulic Fractures

Vincent Tidwell, Sandia National Laboratories, and Mark Parker, SPE, Halliburton Energy Services

This paper was prepared for presentation at the 1996 SPE Annual Technical Conference and Exhibition held in Denver, Colorado, U.S.A., 6-9 October 1996.

Abstract

Laboratory experiments were conducted to physically investigate the processes governing stimulation fluid displacement from hydraulic fractures. Experiments were performed on two scales: meter-scale in a 1500 cm^2 sand pack and core-scale in a 65 cm^2 API linear conductivity cell. High-resolution light transmission imaging was employed at the meter-scale to visualize and quantify processes governing fluid displacement. For comparison, complimentary tests were performed using an API conductivity cell under ambient test conditions and at elevated closure stress. In these experiments viscous fingering and gravity drainage were identified as the dominant processes governing fluid displacement. Fluid viscosity was found to dictate the relative importance of the competing displacement processes and ultimately determine the residual liquid saturation of the sand pack. The process by which fluid displacement occurs was seen to effect the shape of both the gas and liquid phase relative permeability functions. Knowledge of such viscosity/relative permeability relationships may prove useful in bounding predictions of post-stimulation recovery of gels from the fracture pack.

Introduction

Hydraulic fracturing is an accepted and well-documented technique to stimulate production from gas reservoirs; however, gas productivity and recoverable reserves are often impaired by poor recovery of stimulation fluids from the reservoir and hydraulic fracture. Design of enhanced stimulation fluid recovery strategies is complicated by the complexities inherent to the fluid/reservoir system and processes governing fluid displacement. Factors influencing system response include: viscous fingering, capillary trapping, filter cake build-up, gel leak-off, and proppant pack/reservoir heterogeneity.

In efforts to better predict post stimulation behavior of hydraulically fractured gas wells, investigators have demonstrated the ability to physically model the fracture with proppant packs under simulated reservoir conditions of stress and temperature[1-2]. Such experiments have identified gelling agent type[3], gel viscosity[4] (i.e., extent of fluid breaking), insoluble polymer residue[5], non-Darcy flow[6], and closure stress[7] as effecting post stimulation fracture permeability. The extent of fracture permeability damage has been reported to range from minimal to near complete plugging of the fracture. Further work has been done to elicit total fracture/reservoir system response by including dynamic fluid loss processes[8-10]. One limitation common to all is that experiments have been routinely conducted on core-scale samples using methods that only provide information on integrated system response. From such data it is difficult to uniquely discern the basic processes governing fluid displacement.

Numerical experimentation has also been employed to investigate the displacement of stimulation fluids from hydraulically fractured reservoirs. Numerical simulations offer the advantage of being able to investigate the coupled behavior between the hydraulic fracture and invaded reservoir at the scale of interest. A variety of simulators have been used to investigate a wide range of issues. van Poollen[11] investigated the effects of fracture orientation and fracture length on gel recovery from hydraulic fractures, while Tannich[12] evaluated the effects of relative permeability reduction, liquid holdup in the well tubulars, and non-Darcy gas flow. Holditch[13] extended this work by investigating the combined effects of formation permeability damage and relative permeability damage in the invaded matrix. Montgomery et al.[14] and Sherman et al.[15] considered the effects of fracture conductivity, formation damage to the fracture face, and relative permeability hyseresis in the invaded zone. Other studies have shown unbroken fracture fluids can significantly lower gas reserves, reduce gas flow rates, and delay peak gas production rates by weeks or months[16]. Inherent to each of these studies are a variety of modeling assumptions necessitated by lack of data on the fracture and/or reservoir, computational constraints, and by a limited understanding of the basic processes governing fluid displacement.

This work was supported by the United States Department of Energy under Contract DE-AC04-94AL85000.

In efforts to better understand the basic processes governing stimulation fluid displacement and how such processes might be incorporated into predictive models, a series of laboratory experiments have been conducted. These studies differ from conventional laboratory testing in that high resolution light transmission imaging[17] is employed to visualize and quantify displacement processes in thin but extensive (60 by 25 cm) test systems. As the visualization experiments are constrained to operation under ambient test conditions, complimentary core-scale studies using an API linear conductivity cell are performed that allow testing under simulated reservoir conditions of temperature and closure stress.

In this paper we focus our attention on displacement processes occurring within the plane of the hydraulic fracture. Following a description of the laboratory methods we present the results of experiments in which the effects of fluid viscosity, test system scale, differential pressure, and closure stress on fluid recovery from a simulated hydraulic fracture are systematically investigated. From these results the basic processes governing stimulation fluid displacement are identified and their effect on the gas and liquid phase relative permeability functions is explored.

Methods

Laboratory experiments were conducted to investigate recovery processes operating in the plane of the hydraulic fracture. Complementary experiments are performed at both the core- and meter-scale. Core-scale tests allow investigation of displacement processes under simulated reservoir temperatures and fracture closure stresses; however, these tests yield only integrated system response making it difficult to uniquely discern the governing displacement processes. For this reason, meter-scale tests utilizing high resolution imaging techniques are employed to visualize and quantify the processes governing liquid displacement; however, the visualization experiments are currently constrained to ambient test conditions.

Testing of fluid displacement under simulated reservoir conditions was conducted with a modified API linear conductivity cell[1] (Figure 1). The test cell consists of a metal housing that holds two 18 by 4 by 0.6 cm rock slabs separated by a thin (~0.6 cm) sand pack. In these tests Berea Sandstone was used as the contact surface for the 20/40 mesh Ottawa sand pack. The closure stress on the sand pack was controlled with a hydraulic jack set in a four-post load frame. The orientation of the fracture in the test cell was vertical. The test cell was initially saturated with the test liquid (see Table 1), which was then displaced from the pack using nitrogen gas supplied at a constant flow rate with a Hastings Mass Flow Controller. Gas flow rates used ranged from 100 sccm (cm^3/min. at standard conditions) to 500 sccm. The mass of water displaced was measured with a Mettler electronic balance. Differential pressure in the pack was measured with a Honeywell Smart Transducer calibrated for a 250 cm water column. Test cell temperature was controlled with a EuroTherm temperature controller. All test data were monitored and recorded with a computer data acquisition system.

Experiments aimed at visualizing liquid displacement processes occurring in the hydraulic fracture were conducted in a 60 by 25 by 0.6 cm test cell (Figure 2). The test cell was constructed of two 1.9 cm thick glass plates spaced 0.6 cm apart with flow manifolds secured at each end. Gas was introduced into the test cell through the inflow manifold which distributed the flow along the height of the chamber by means of four 6 cm long metal porous plates. The discharging gas and liquid flow through the outflow manifold comprised of a simple screened slot with a single outlet at the top. Prior to each experiment the chamber was homogeneously packed[18] with clean 20/40 mesh Accusand. Experiments were conducted with the chamber oriented vertically and flow directed parallel to the long axis of the chamber.

To visualize and quantify liquid displacement, the test cell was placed in front of a controlled, high-intensity light source. The intensity of light passing though the sand pack at any point is directly related to the liquid saturation integrated over the thickness of the pack. As the liquid saturation increases, the transmitted light intensity also increases because of the closer matching of the index of refraction of the sand and water relative to the sand and air. The transmitted light intensity field was imaged using a high-resolution, water-cooled CCD camera. In this way, the transmitted light intensity field was digitized into an array of 1024 by 1024 pixels (<mm^2 spatial resolution) with a dynamic range of 4096 gray levels. Each grey level value was then converted to liquid saturation through a two-step process. The first step adjusted the image to correct for variation in image source intensity though use of a stepped optical density wedge included in each image. In the second step, the adjusted grey level values were converted to saturation using a functional relationship based on light refraction theory.[17]

The visualization experiments were initiated by measuring the permeability of the dry sand pack. The pack was then saturated with de-aired liquid by gravity fill from the bottom of the chamber. The displacement test began with the liquid being driven from the test chamber using nitrogen gas supplied through the inlet manifold at a prescribed pressure. During this time, transmitted light images were collected at 15 second intervals (time required to save data file to disk) to capture the transient liquid displacement behavior. Concurrent measurement of the gas and liquid produced by the chamber was performed. The mass of liquid produced was measured with a Mettler electronic balance, while a Sierra Instruments (0-20,000 sccm) mass flow meter measured the gas production and two Sensotec differential pressure transducers (0-100 KPa) measured the inlet and outlet gas pressure. Tests were allowed to proceed until liquid production from the cell ceased and steady gas production was achieved.

Results

A suite of laboratory experiments were conducted to investigate the basic processes governing stimulation fluid displacement from a simulated hydraulic fracture. Concurrent experiments were conducted at two very different scales using the flow visualization test system and the API linear conductivity cell. In these experiments the effects of fluid viscosity, the scale of the experiment, differential pressure, and fracture closure stress on liquid displacement were

systematically investigated. Although this study does not provide an exhaustive investigation of the full parameter space, the selected variables are believed to capture the first-order effects.

Viscosity Effects. In the first series of experiments the effects of fluid viscosity on liquid displacement were explored. A total of four tests were performed, each test using a liquid with different viscosity (Table 1). Test fluids included a 0.48 wt% Hydropropyl Guar (HPG) (35 centipoise [cp]), 0.24 wt% HPG (17 cp), 0.48 wt% HPG with enzyme breaker (2.2 cp), and de-ionized water (1 cp). Tests were performed under room temperature using a homogeneous sand pack and a prescribed gas phase pressure gradient (dp/dx) of 5.7 cm/cm (consistent with conditions commonly encountered in field stimulation projects).

Figure 3 presents three, 2-D liquid saturation fields tracking the transient displacement of the 0.48 wt% HPG gel ("high" viscosity test case) from the flow visualization test chamber. In these images gas flow is from right to left and black corresponds to full liquid saturation which grades through various shades of grey with white denoting an air-dry sand pack. From the first image it is apparent that gel displacement is governed by viscous fingering. The path of the fingers is tortuous but effectively horizontal. As the fingers approach the left side of the chamber they expand and coalesce in response to the fluid's access to the outflow boundary. At steady-state (Figure 3c) a relatively large fraction of the gel remains trapped in the sand pack with only a slight vertical trend evident in the saturation distribution.

A somewhat different response is noted for the test employing water representing the low viscosity endmember (Figure 4). As before viscous fingering occurred during the early phase of displacement (Figure 4a); however, the fingers have a distinct vertical component to their orientation. The fingers were also noted to move more quickly across the test system. In fact, only a diffuse outline of the fingers is left in this first image of the test sequence, thus making it difficult to discern the fingers. With time, the liquid remaining in the sand pack becomes increasingly concentrated in a wedge located near the lower outflow boundary (Figure 4c). The upper interface of the wedge exhibits a parabolic shape characteristic of a density stratified system in which the lighter fluid is flowing over a stationary or slowly-moving denser fluid. The residual liquid saturation is also noted to be considerably lower than measured in the 0.48 wt% HPG test case.

The tests cases employing the 0.24 wt% HPG gel and the 0.48 wt% HPG gel with enzyme breaker display an intermediate or transitional behavior relative to the "high" and low viscosity test cases. Such behavior is evident in the orientation of the viscous fingers. As the fluid viscosity decreases the vertical component of the finger orientation is seen to increase. A transitional trend is also exhibited with respect to the vertical distribution of the residual liquid saturation in the chamber. As the fluid viscosity decreases, increased density stratification or liquid drainage occurs. That is, the formation of a "saturated" wedge (as described above) near the lower outflow boundary is much more pronounced in the case of the lower viscosity gel. Transitional behavior is also seen in the effective residual gel saturation which increases with increasing fluid viscosity.

From this series of experiments, the basic processes governing liquid displacement can be readily distinguished. As expected, viscous fingering and gravity drainage are the dominant displacement processes. Also as expected, the fluid viscosity ultimately defines the relative importance of the competing processes and their time scales. As such, displacements dominated by viscous forces are characterized by persistent fingers and limited density stratification of the fluids. However, as fluid viscosity decreases gravitational forces become more prominent as indicated by significant vertical segregation of the fluid phases (growth of a "saturated" wedge).

The viscous fingers measured in the early phase of each test were found to be in good agreement with linear stability theory. Analyses were conducted using the model of Chuoke et al.[19]. The permeability of the media used in the calculations was based on dry sand pack measurements (1 darcy), while the gas phase flow velocities were determined from Darcy flow calculations and on a pore-volume-per-time basis. Fluid properties used in the calculations were measured directly and are given in Table 1. According to the resulting analysis, the system is inherently viscous unstable over the entire range of viscosities tested. This is in agreement with our results in which viscous fingers developed in all four test cases. Using equation 24 of Chuoke et al.[19] the average spacing between fingers is predicted to be consistent, approximately 2 cm apart. In this analysis the effective interfacial tension was assumed to be equal to the interfacial tension of the fluid which will tend to underestimate actual finger spacing. In the four test cases, finger spacing was found to be relatively consistent on the order of 1-2 cm.

The transient and steady-state displacement behavior integrated over the entire simulated hydraulic fracture is quantified in the liquid production profiles. In Figure 5 the mass of liquid produced, normalized by the initial mass of liquid in the chamber (i.e., the effective gas saturation of the test cell), is plotted verses time for the four test cases. From this plot it is evident that the effective gas saturation is inversely related to fluid viscosity. The residual gas saturation is seen to differ by 25% between the "high" and low viscosity test cases. Comparison of the liquid production curves also reveals a significant difference in the period of time required for the system to reach steady-state. The time to reach steady-state for the 0.48 wt% HPG and water test cases differs by almost an order of magnitude.

Because the basic shape of the gas production profiles are essentially mirror images of the liquid production profiles they are not included here. However, there are important differences in absolute terms that bear mentioning. The gas production rates, normalized by the dry pack production rate, measured at residual saturation are 37.5%, 40%, 39%, and 40% for the 0.48 wt% HPG, 0.24 wt% HPG, 0.48 wt% HPG with breaker, and water respectively. Thus, only minimal differences in the steady-state gas phase production rates is exhibited; however, the time to reach these rates differ, following a patter

similar to that shown in the liquid production profiles (Figure 5).

System Scale Effects. Comparison of the liquid production profiles measured with the API linear conductivity cell and flow visualization test system provide insight into the effects of scale on measured system response. Figure 6 presents a comparison between the liquid production profiles for the two test systems. To facilitate comparison, the time scales have been normalized to account for differences in the lengths of the test cells. Results for two experiments are presented; one employing 0.48 wt% HPG at a dp/dx of 5.7 cm/cm and the other de-ionized water at a dp/dx of 1.5 cm/cm (lower differential pressure presented above).

In both cases, residual saturations measured by the two systems are in reasonable agreement, ~5% difference (possibly due to the difference in sands used in the two test systems). However, the time to reach residual saturation is very different with the API cell, which recorded much earlier displacement times. This discrepancy is attributable to the fact that the API test cell is of a comparable size to the average viscous finger spacing. For this reason the API test cell will underrepresent the effects of viscous fingering and hence tend to underestimate the time required to reach residual saturation. As such, particular care must be taken when using the results of core-scale tests such as the API conductivity cell to predict displacement behavior for larger scale systems.

Also worth noting is the cause of the stepped behavior evident in the de-ionized water production curve for the flow visualization test cell. This behavior is the result of the low dp/dx applied to the test cell, which was insufficient to maintain flow across the entire inflow manifold during early phases of the test. Once enough water was displaced the gas pressure was sufficient to initiate flow through the bottom two porous plates of the inflow manifold thus causing the resurgence in water production evident at 1200 seconds.

Differential Pressure Effects. Experiments have also been performed to investigate the effects of differential pressure on liquid displacement. Two experiments using a 0.48 wt% HPG gel were performed with a dp/dx of 5.7 and 8.1 cm/cm. Experiments employing de-ionized water as the test fluid were also performed in which displacement behavior was measure at a dp/dx of 1.5, 2.8, and 5.7 cm/cm. Figure 7 presents the liquid production profiles for these five tests.

To aid in the interpretation of these results, the capillary pressure curve for the 20/40 mesh sand using de-ionized water as the test fluid was measured (Figure 8). The curve was measured by allowing the flow visualization test chamber to gravity drain from an initially saturated condition (a water potential of zero was maintained at the bottom of the chamber, which was oriented with its long axis vertical). At steady-state the fluid saturation (as measured by the transmitted light technique) averaged across the width of the chamber was plotted verses chamber height. The curve is very flat reflecting the narrow grain size distribution of the sand pack. A higher viscosity fluid would be expected to behave in much the same manner but with a higher air entry pressure and residual saturation.

With respect to the test cases employing water as the test fluid, changes in the differential pressure are seen to effect water production in two ways. First, the time required to reach steady-state is noted to increase as dp/dx decreases. This behavior simply reflects the reduced energy available to drive fluid displacement. The second effect relates to differences in the residual gas saturation. The test cases performed at a dp/dx of 2.8 and 5.7 cm/cm achieve similar residual saturations while the test performed at a dp/dx of 1.5 cm/cm is approximately 15% lower. As the capillary tension for the three test cases are 350, 175, and 90 cm of water respectively, all three should reach a residual gas saturation of approximately 80% (Figure 8). The test case performed at a dp/dx of 1.5 cm/cm fails to reach this point due to the persistence of a "saturated" wedge. Although a "saturated" wedge was noted to form in all three tests, their size at steady-state remained small with respect to the overall size of the chamber in all but the lowest dp/dx case. Given the density stratified nature of the flow field and configuration of the outflow boundary, the size of the "saturated" wedge will be inversely related to dp/dx as seen here. Similar boundary and flow conditions may be experienced in the field when fluid viscosities and bottom hole flowing pressures are low. In such situations careful consideration of the potential for water blockage due to the formation and persistence of a "saturated" wedge should be made.

In contrast, changes in differential pressure are seen to have almost no effect in the tests employing the 0.48 wt% HPG gel. Minimal differences in the time scales of the displacment process (not visible at the scale plotted) occur owing to the relatiely small range in dp/dx and the low mobility of the gel. Also, slight differences in the residual saturation are noted. The registered difference being attributed to experimental error. Although not seen here, threshold effects will also occur in the case of high viscosity fluids where displacement is dominated by viscous fingering. In such cases, the threshold will be simply defined by the pressure required to overcome the viscous forces of the gel.

Fracture Closure Stress Effects. The effects of fracture closure stress on stimulation fluid displacement were investigated using the API linear conductivity cell. Closure stress effects were evaluated with sand packs filled with de-ionized water and 0.48 wt% HPG. Results of the test show that at a gas flow rate of 100 sccm and 6.9 MPa closure stress the effective gas saturation is approximately 60% in the water filled pack (Figure 9). By increasing the closure stress to 13.8 MPa the effective gas saturation fell to 52% while at a closure stress of 27.6 MPa it falls to about 45%. The gel filled packs showed similar results. At 100 sccm and 6.9 MPa closure stress the effective gas saturation is nearly 60%. At 13.8 MPa closure stress the effective gas saturation falls to approximately 30% and at 27.6 MPa closure stress it falls to about 25%.

For the test case using water, we see a distinct decrease in the effective gas saturation with increasing closure stress. This

behavior is attributable to the closure stress reducing the overall pore size of the sand pack. The reduction in pore size in turn changes the capillary pressure characteristics of the sand pack. From the data we also note that the gas saturation is quite low even at a closure stress of 6.9 MPa. This low value is primarily the result of the threshold effect discussed previously.

Tests performed using the gel-saturated sand packs also exhibit a decrease in the effective gas saturation with increasing closure stress; however, the effect is much more pronounced than in the water saturated sands. Such behavior is expected given the lower mobility of the gel relative to water.

Discussion

A basic understanding of the processes governing stimulation fluid displacement from the hydraulic fracture is important for both the pre-treatment design of stimulation projects as well as for post-treatment calculations of the effective fracture dimensions and recoverable gas reserves. From the results presented above it is clear that models used in predicting gel displacement must account for the effects of gravity drainage and viscous fingering. Gravity drainage can easily be treated by explicitly modeling the vertical dimension of the stimulation project; however, vertically integrated flow models are generally required to reduce the computational burden posed by these calculations. Viscous fingering effects on gel recovery can be approximated through the use of models such as the ones proposed by Buckley and Leverett[20] and Pope et al.[21]. An alternative and very simple approach would be to bound the effects of gravity drainage and viscous fingering through careful formulation of the relative permeability functions.

Based on the gas and liquid production profiles measured during the flow visualization tests, the gas phase (Figure 10) and liquid phase (Figure 11) relative permeability functions for the simulated fracture pack have been calculated. Shown are the curves for the 0.48 wt% HPG gel, 0.24 wt% HPG gel, and water test cases, all of which were measured at a dp/dx of 5.7. Inspection of the gas phase data reveals that the relative permeability k_{rel} follows a simple power law relation,

$$k_{rel} = \alpha\left(S_{eff}\right)^{n} \quad \ldots\ldots(1)$$

where α is a multiplicative factor, n is the power coefficient and, S_{eff} is defined as

$$S_{eff} = \left(S - S_r\right) \Big/ \left(S_s - S_r\right) \quad \ldots\ldots(2)$$

where S is the measured gas phase saturation of the sand pack, and the subscripts r and s refer to the gas saturation under residual and saturated conditions respectively. Note that α in Equation 1 is simply equal to k_{rel} when S_{eff} is 1. The liquid phase k_{rel} functions exhibit a dual behavior following a linear relationship during early times and a power law relation (Equation 1) at later times. Model parameters for all six curves are given in Table 2.

In the case of both the gas and liquid phase k_{rel} functions the power coefficient is noted to increase with increasing fluid viscosity. In fact, the power coefficient is seen to be linearly related to the fluid viscosity for both the liquid and gas phase curves. However, the degree to which the power coefficient varies is much greater in the case of the liquid phase. The increasing curvature of the k_{rel} function reflects the growing persistence of viscous fingerings with increasing fluid viscosity. That is, as the fluid viscosity increases viscous fingers persist longer during the displacement process thus increasing tortuosity and decreasing permeability (the gas phase being much less sensitive to the increased tortuosity).

A complicating factor in modeling the k_{rel} functions is the discontinuous nature of the liquid phase curves. The discontinuity between the linear and power law behavior simply marks the point at which the liquid phase is no longer continuously connected to the test cell outlet.

The measured viscosity/relative permeability relationship can be used as a guide in making bounding calculations concerning gel recovery from the hydraulic fracture. That is, a series of numerical simulations can be performed employing a range of power coefficients, selection of which can be guided by the results given here. The results of the analysis will provide a basis for predicting system response for a range of potential post-stimulation gel viscosity conditions. Although it must be recognized that the viscosity/power coefficient relation in absolute terms will vary according to the specific conditions of the stimulation projects. Hence, the result of such numerical analysis must be viewed in terms of bounding potential system response. The viscosity/power coefficient relation should also not be extended much beyond the range measured here as it is uncertain over what range the linearity of the function will hold. Additional experimental work is need to assess this relationship at elevated viscosities.

Conclusions

A significant portion of the gel used in hydraulic fracturing treatments remain trapped in the fracture and formation impeding production throughout the life of the well. Engineering of enhanced recovery strategies requires an improved understanding of the processes governing stimulation fluid displacement. To support this need, a series of laboratory experiments have been performed that focus on displacement from the hydraulic fracture. These experiments integrate industry standard core-scale testing techniques with unique high-resolution imaging capabilities that allow visualization and quantification of liquid displacement from thin, 2-dimensional sand packs. Key findings of these tests include the following:

1) Tests confirm that viscous fingering and gravity drainage are the primary processes governing gel displacement from the hydraulic fracture. Of no surprise was the finding that fluid viscosity ultimately dictates the mode and total extent of gel displacement; however, the magnitude of this effect was not fully appreciated. For a relatively small increase in fluid viscosity (1 to 35 cp) we noted the residual liquid saturation to

increase 25% while the time to reach residual saturation increased 10 fold.
2) Significant scale effects were noted between the API cell and flow visualization cell. These differences are attributed to the limited size of the API cell in which it is difficult to fully capture the effects of viscous fingering and gravity drainage on liquid displacement.
3) In the visualization experiments we also noted the formation of a "saturated" wedge near the lower outflow boundary when low viscosity fluids were used. The persistence of such features may be of importance in stimulation projects where post-stimulation fluid viscosities are low and bottom-hole flowing pressures are low.
4) As expected, increasing closure stress was found to reduce liquid production. Effects were noted to be more pronounced for the higher viscosity fluids.
5) The gas and liquid phase relative permeability functions were noted to change in response to changes in the governing displacement process. The k_{rel} curves were noted to follow a power law relation where the power coefficient was linearly related to the fluid viscosity. This simple relation may prove to be a useful tool for bounding predictions of gel recovery from the hydraulic fracture.

Acknowledgments

The authors would like to express their appreciation to Will Peplinski, Kerim Martinez, and Anthony Chavez for their help in performing the flow visualization experiments and in the reduction of the image data, and to Mickey Stewart for his help in conducting the experiments in the API conductivity cell. This work was in part supported by the U.S. Department of Energy, Natural Gas and Oil Technology Partnership Program.

References

1. API RP 61: *Recommended Practices for Evaluating Short Term Proppant Pack Conductivity*, First Edition, October 1989, American Petroleum Institute (1989).
2. McDaniel, B.W.: "Conductivity Testing of Proppants at High Temperature and Stress," paper SPE 15067 presented at the SPE California Regional Meeting, Oakland, CA, April 1986.
3. Almond, S.W.: "Factors Affecting Gelling Agent Residue Under Low Temperature Conditions," paper SPE 10658 presented at the Formation Damage Control Symposium, Lafayette, LA March 24-25, 1982.
4. Almond, S.W., and Bland, W.E.: "The Effect of Break Mechanism on Gelling Agent Residue and Flow Impairment in 20/40 Mesh Sand," paper SPE 12485 presented at the Formation Damage Control Symposium, Bakersfield, CA, Feb. 13-14, 1984.
5. Cooke, C.E.: "Conductivity of Fracture Proppants in Multilayers," *Journal of Petroleum Techechnology* (Sept. 1973) 1101.
6. Roodhart, L.P., Kulper, T.O.H, and Davies, D.R.: "Proppant-Pack and Formation Impairment During Gas-Well Hydraulic Fracturing," *SPE Production Engineering* (November 1988) 438.
7. Kim, C.M., and Losacano, J.A.: "Fracture Conductivity Damage Due to Crosslinked Gel Residue and Closure Stress on Propped 20/40 Mesh Sand," paper SPE 14436 presented at the 60th Annual Technical Conference and Exhibition, Las Vegas, NV, Sept. 22-25, 1985.
8. McDaniel, B.W.: "Realistic Fracture Conductivities of Proppants as a Function of Reservoir Temperature," paper SPE/DOE 16453 presented at the SPE/DOE Symposium on Low Permeability Reservoirs, Denver, CO. May 18-19, 1987.
9. Penny, G.S.: "An Evaluation of the Effects of Environmental Conditions and Fracturing Fluids Upon the Long-Term Conductivity of Proppants," paper SPE 16900 presented at the 62nd Annual Technical Conference and Exhibition, Dallas, TX, Sept. 27-30, 1987.
10. Parker, M.A., and McDaniel, B.W.: "Fracturing Treatment Design Improved by Conductivity Measurements Under In-Situ Conditions," paper SPE 16901 presented at the 62nd Annual Technical Conference and Exhibition, Dallas, TX, Sept. 27-30, 1987.
11. van Poollen, H.K., "Do Fracture Fluids Damage Productivity," *The Oil and Gas Journal* (May, 1957) **55**, 120.
12. Tannich, J.D.:"Liquid Removal from Hydraulically Fractured Gas Wells," *Journal of Petroleum Technology* (November, 1975) 1309.
13. Holditch, S.A.: "Factors Affecting Water Blocking and Gas Flow from Hydraulically Fractured Gas Wells," *Journal of Petroleum Technology* (December, 1979) 1515.
14. Montgomery, K.T., Holditch, S.A., and Berthelot, J.M.: "Effects of Fracture Fluid Invasion on Cleanup Behavior and Pressure Buildup Analysis," paper SPE 20643 presented at the 1990 Annual Technical Conference and Exhibition, New Orleans, LA, Sept. 23-26.
15. Sherman, J.B., and Holditch, S.A.: "Effects of Injected Fracture Fluids and Operating Procedures on Ultimate Gas Recovery," paper SPE 21496 presented at the 1991 SPE Gas Technology Symposium, Houston, TX, Jan. 23-25.
16. Voneiff, G.W., Robinson, B.M., and Holditch, S.A.: "The Effects of Unbroken Fracture Fluid on Gas Well Performance," paper SPE 26664 presented at the 1993 Annual Technical Conference and Exhibition, Houston, TX, Oct. 3-6.
17. Tidwell, V. C., and Glass, R.J.:" X-ray and Visible Light Transmission for Laboratory Measurement of Two-Dimensional Saturation Fields in Thin-Slab Systems," *Water Resources Research*, (1994) 2873.
18. Glass, R.J., Steenhuis, T.S., and Parlange, J.-Y.: "Wetting Front Instability, 2, Experimental Determination of Relationships Between System Parameters and Two-Dimensional Unstable Flow Field Behavior in Initially Dry Porous Media," *Water Resources Research* (1989) 1195.
19. Chuoke, R.L., vonMeurs, P., van der Poel, C.: "The Instability of Slow, Immiscible, Viscous Liquid-Liquid Displacements in Permeable Media," *Trans. AIME* (1959) **216**, 198.

20. Buckley S.E. and Leverett, M.C.: "Mechanism of Fluid Displacement in Sands," *Petroleum Technology* (1941) 107.
21. Pope, D.S., Leung, L.K-W., Gulbis, J., and Constien, V.G.: "Effects of Viscous Fingering on Fracture Conductivity," SPE 28511 presented at the 89th Annual Technical Conference and Exhibition, New Orleans, LA , Sept., 25-28, 1994.

Table 1: Physical properties of fluids used in laboratory tests.

Fluid	Viscosity (centipoise)	Specific Gravity
Gelled fluid (0.48 wt% HPG)*	35	1.02
Gelled fluid (0.24 wt% HPG)*	17	1.02
Gelled fluid with enzyme breaker† (0.48 wt% HPG)*	2.2	1.02
Water	1.0	1.00

* 2% KCl by weight used to buffer solution
† A break time of 24 hr. at room temperature was allowed

Table 2: Model parameters for gas and liquid phase relative permeability functions.

Fluid	Gas Phase		Liquid Phase		S_r	S_s
	α	n	α	n		
0.48 wt% HPG	0.38	2.3	0.020	-1.5	0.54	0.0
0.24 wt% HPG	0.40	2.1	0.015	-4.0	0.68	0.0
Water	0.40	1.9	0.015	-6.5	0.80	0.0

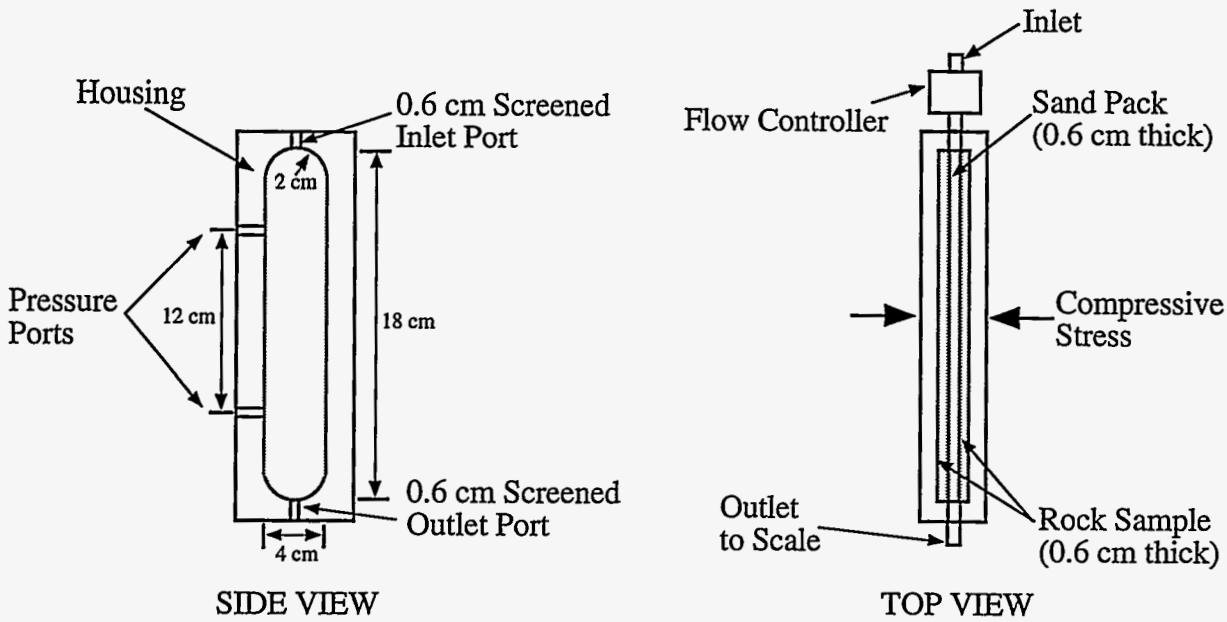

Fig. 1--Schematic of API linear conductivity test system.

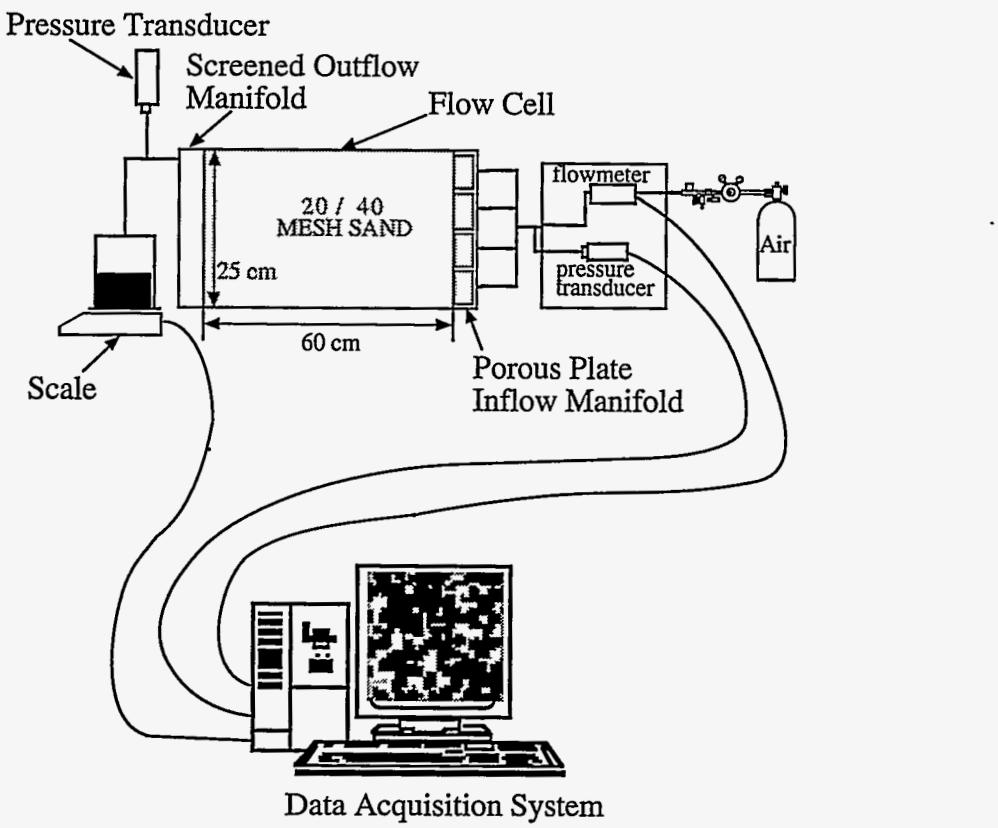

Fig. 2--Schematic of the flow visualization test system. Visualization and quantification of displacement processes is accomplished by mounting the test cell in front of a high intensity light source and subsequently imaging the 2-D transmitted light intensity field with a high resolution CCD camera.

Fig. 1–Schematic of API linear conductivity test system.

Fig. 2–Schematic of the flow visualization test system. Visualization and quantification of displacement processes is accomplished by mounting the test cell in front of a high-intensity light source and digitizing the 2-dimensional transmitted light intensity field with a high-resolution CCD camera.

a) t = 40 Seconds

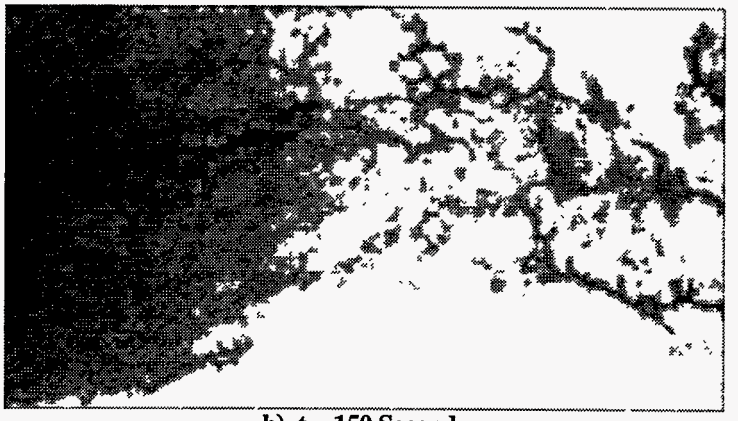

b) t = 150 Seconds

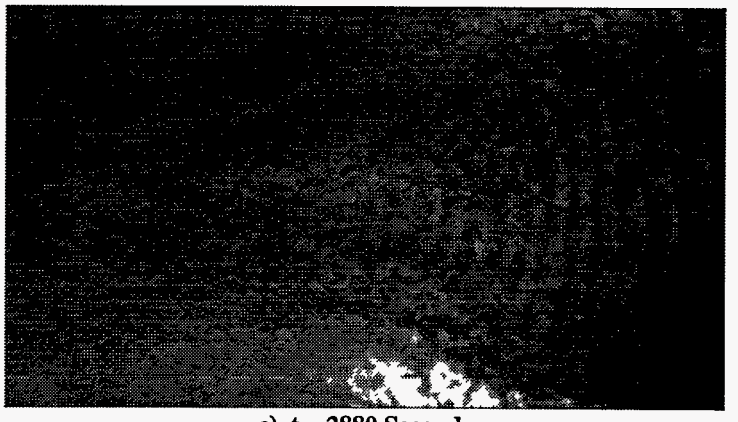

c) t = 2880 Seconds

Fig. 3–Displacement of 0.48 wt% HPG from the 60 by 25 by 0.6 cm sand filled test cell. The three images show the progression of displacement in time. Gas flow is from right to left. The grey scale grades from light grey indicating full liquid saturation to black for an air-dried sand pack. Viscous fingering is seen to dominate the displacement process.

Fig. 3–Displacement of 0.48 wt% HPG from the 60 by 25 by 0.6 cm flow visualization test cell. The three images show the progression of displacement in time. Gas flow is from right to left. The grey scale grades from light grey indicating full liquid saturation to black for an air-dried sand pack. Viscous fingering is seen to dominate the displacement process.

a) t = 15 Seconds

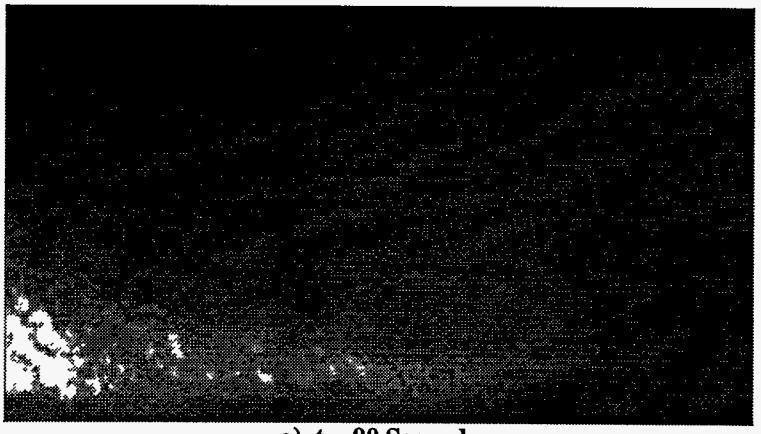

a) t = 90 Seconds

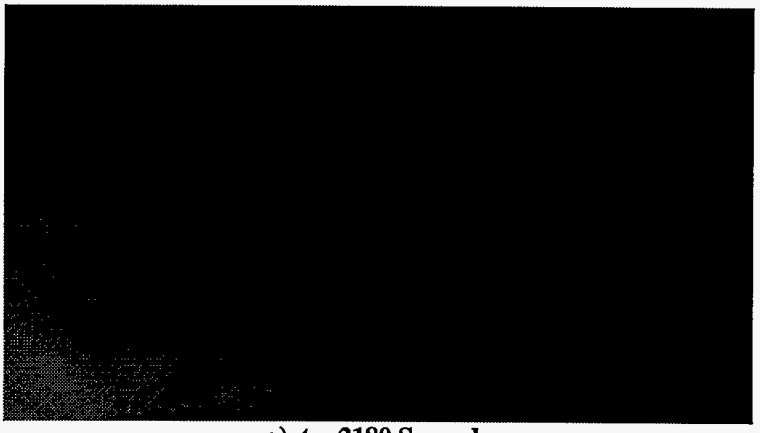

a) t = 2180 Seconds

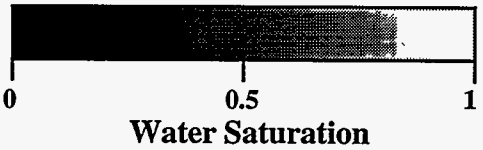

Fig. 4–Displacement of water from the 60 by 25 by 0.6 cm sand filled test cell. In this test viscous fingers form early in the displacement process. Gravity drainage is also seen to play a critical role in displacement as indicated by the density segregation of the fluids and the formation of a "saturated" wedge near the lower outflow boundary of the test cell.

Fig. 4–Displacement of water from the 60 by 25 by 0.6 cm flow visualzation test cell. Both viscous fingering and gravity drainge processes are responsible for the displacment behavior seen here. Gravity drainage is evident from the density segregation of the fluids and the formation of a "saturated" wedge near the lower outflow boundary of the test cell.

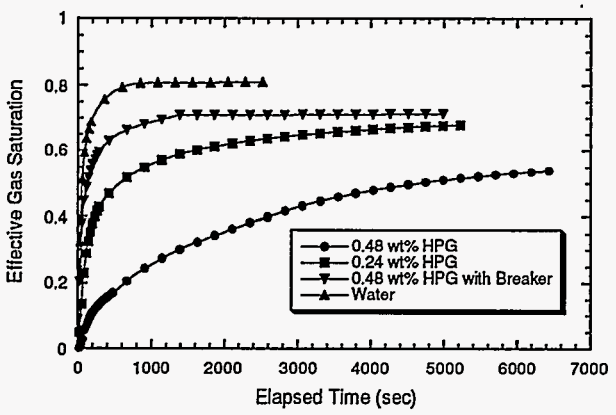

Fig. 5–Liquid production profiles for displacement experiments conducted in the flow visualization test cell employing 0.48 wt% HPG, 0.24 wt% HPG, 0.48 wt% HPG with enzyme breaker, and water. Liquid production was normalized by the initial mass of fluid in the chamber to yield the effective gas saturation. The effective gas saturation is noted to increase with decreasing fluid viscosity while the time to reach residual saturation is seen to decrease.

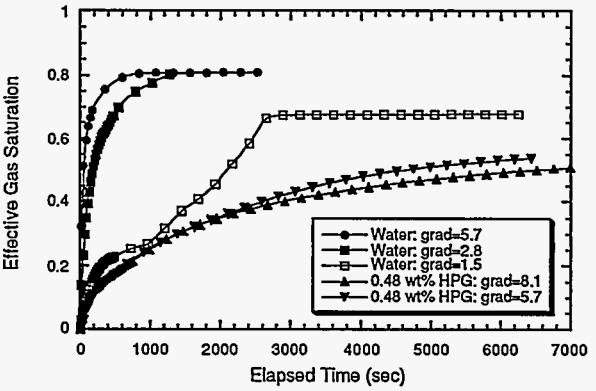

Fig. 7–Differential pressure effects on liquid production from the flow visualization test cell. Tests employing water were performed with a dp/dx of 1.5, 2.8, and 5.7 cm/cm. Tests using 0.48 wt% HPG were performed at a dp/dx of 5.7 and 8.1 cm/cm. Differential pressure effects are minimal in the case of the viscous gel while a threshold effect is evident in the test cases using water.

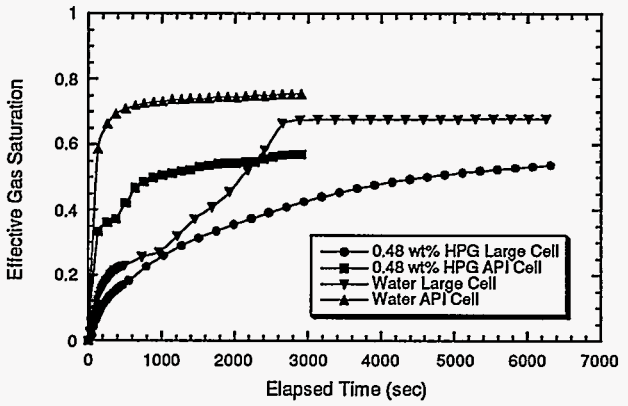

Fig. 6–Comparison of liquid production profiles measured with the API conductivity cell and the flow visualization test chamber for displacement experiments employing 0.48 wt% HPG and water. Time scales were normalized to account for differences in the lengths of the test cells. Tests conducted at the two different scales are similar in terms of the measured residual saturations but differ significantly in the time required to reach these limits.

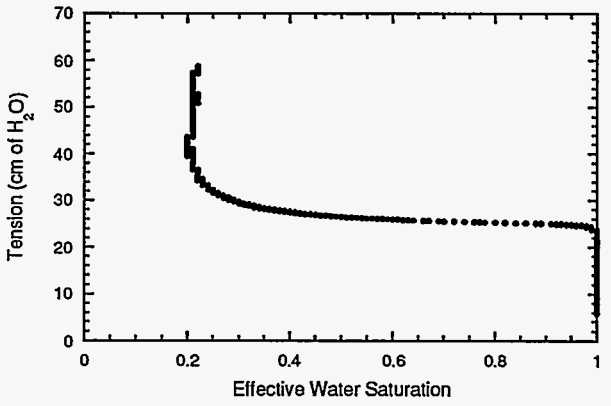

Fig. 8–Capillary pressure curve for the 20/40 mesh sand measured with water. The relatively flat nature of the curve reflects the narrow grain size distribution.

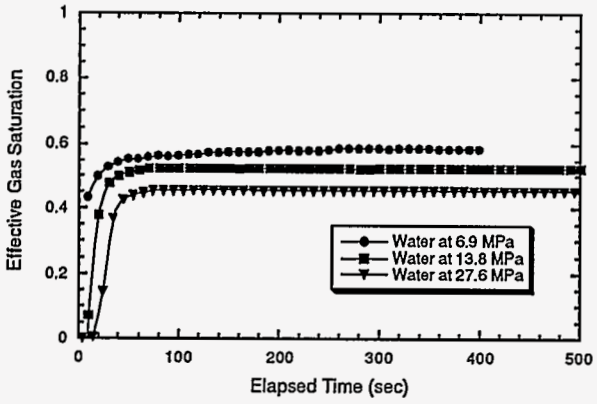

Fig. 9–Closure stress effects on liquid production profiles measured with the API conductivity cell. Test were conducted using sand packs saturated with water at closure stresses of 6.9, 13.8, and 27.6 MPa. In these tests the residual saturation is seen to decrease as a function of increasing closure stress.

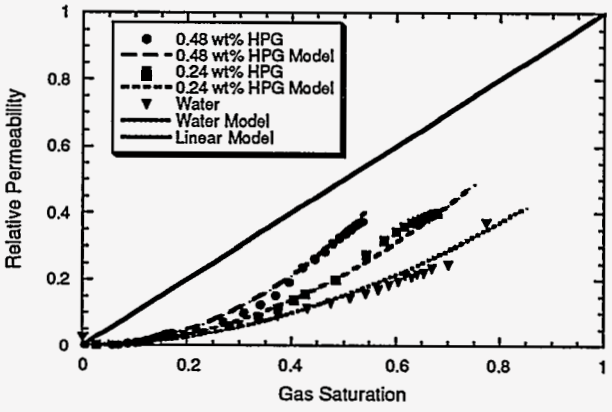

Fig. 11–Gas phase relative permeability functions measured in the flow visualization test cell. Curves for 0.48 wt % HPG, 0.24 wt % HPG, and water are shown. The curves are seen to follow a power law relationship where the power coefficient increases with increasing fluid viscosity.

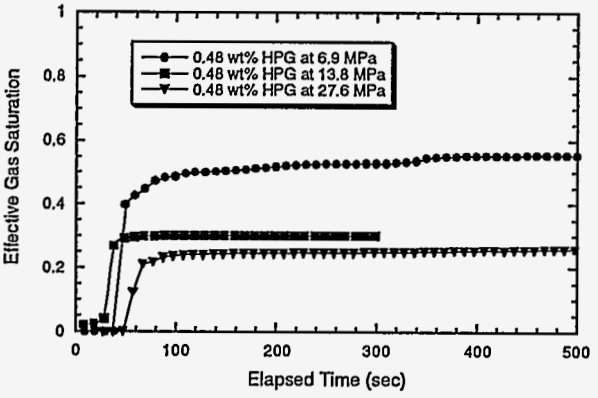

Fig. 10–Closure stress effects on liquid production profiles measured with the API conductivity cell. Test were conducted using sand packs saturated with 0.48 wt% HPG at closure stresses of 6.9, 13.8, and 27.6 MPa. Again, the residual saturation is seen to decrease as a function of increasing closure stress.

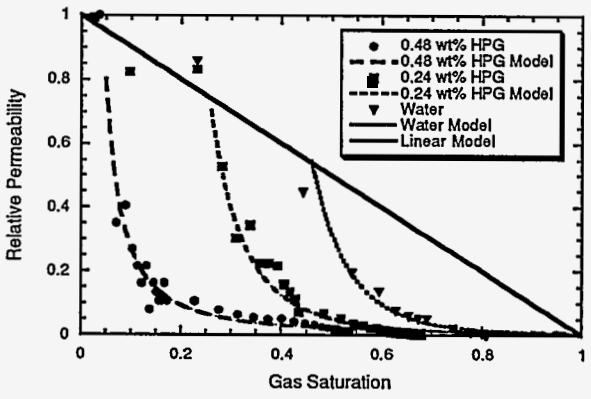

Fig. 12–Liquid phase relative permeability functions measured in the flow visualization test cell. Curves for 0.48 wt % HPG, 0.24 wt % HPG, and water are shown. The curves are seen to initially follow a linear relation with saturation then transition to a power law relation. Again, the power coefficient is found to increases with increasing fluid viscosity.

DISCLAIMER